Charging and Ion Ejection Dynamics of Large Helium Nanodroplets

Exposed to Intense Femtosecond Soft X-Ray Pulses

Catherine A. Saladrigas, ^{1,2} Alexandra J. Feinberg, ³ Michael P. Ziemkiewicz, ^{1,2,a} Camila Bacellar, ^{1,2,b} Maximilian Bucher, ^{4,5,6} Charles Bernando, ^{7,d} Sebastian Carron, ⁸ Adam S. Chatterley, ^{1,2,c} Franz-Josef Decker, ⁵ Ken R. Ferguson, ⁵ Luis Gomez, ³ Taisia Gorkhover, ^{5,6} Nathan A. Helvy, ^{1,9} Curtis F. Jones, ^{3,e} Justin J. Kwok, ^{10 f} Alberto Lutman, ⁵ Daniela Rupp, ^{6,11} Rico Mayro P. Tanyag, ^{3,c} Thomas Möller, ⁶ Daniel M. Neumark, ² Christoph Bostedt, ^{4,5,12,13} Andrey F. Vilesov, ^{3,8,*} and Oliver Gessner^{1,†}

¹Chemical Sciences Division, Lawrence Berkeley National Laboratory, Berkeley, California 94720, USA

²Department of Chemistry, University of California, Berkeley, California 94720, USA

³Department of Chemistry, University of Southern California, Los Angeles, California 90089, USA

⁴ Chemical Sciences and Engineering Division, Argonne National Laboratory, 9700 South Cass Avenue B109, Lemont, IL 60439, USA

⁵ SLAC National Accelerator Laboratory, 2575 Sand Hill Road, Menlo Park, California 94025, USA
⁶ Institute of Optics and Atomic Physics, Technical University of Berlin, Hardenbergstraße 36, 10623 Berlin,
Germany

⁷Department of Physics and Astronomy, University of Southern California, Los Angeles, California 90089, USA

⁸ Department of Physics, California Lutheran University, Thousand Oaks, California, 91360, USA.

⁹Department of Physics, University of California, Berkeley, California 94720, USA

¹⁰Mork Family Department of Chemical Engineering and Materials Science, USC, Los Angeles, California 90089, USA

¹¹ LFKP, ETH Zurich, John-von-Neumann-Weg 9, 8093 Zürich, Switzerland
¹²Paul Scherrer Institut, Forschungsstrasse 111, 5232 Villigen-PSI, Switzerland

¹³LUXS Laboratory for Ultrafast X-ray Sciences, Institute of Chemical Sciences and Engineering, École Polytechnique Fédérale de Lausanne (EPFL), CH-1015, Lausanne, Switzerland

Current Addresses:

^aBall Aerospace, Boulder CO

^b Paul Scherrer Institute, Forschungsstrasse 111, 5232 Villigen-PSI, Switzerland

^c Department of Chemistry, Aarhus University, Langelandsgade 140, 8000 Aarhus C, Denmark

^{*}vilesov@usc.edu

[†]ogessner@lbl.gov

^d School of Information Systems, Binus University, Jl. K.H. Syahdan No. 9, Palmerah, Jakarta Barat 11480 Indonesia

^e State University of New York (SUNY) Adirondack, Queensbury, NY, 12804, USA.

^fDepartment of Materials Science and Engineering, University of Illinois at Urbana-Champaign, 1304 W. Green St., Urbana, IL 61801, USA.

Abstract:

Ion ejection from charged helium nanodroplets exposed to intense femtosecond soft x-ray pulses is studied by single-pulse ion time-of-flight (TOF) spectroscopy in coincidence with small-angle x-ray scattering. Scattering images encode the droplet size and absolute photon flux incident on each droplet, while ion TOF spectra are used to determine the maximum ion kinetic energy, KE, of He_n^+ fragments (n = 1-4). Measurements span He_N droplet sizes between N~ 10^7 and 10^{10} (radii $R_0 = 78-578$ nm), and droplet charges between ~ 9×10^{-5} and ~ 3×10^{-3} e/atom. Conditions encompass a wide range of ionization and expansion regimes, from departure of all photoelectrons from the cluster, leading to pure Coulomb explosion, to substantial electron trapping by the electrostatic potential of the charged droplet, indicating the onset of hydrodynamic expansion. The unique combination of absolute x-ray intensities, droplet sizes, and ion KE on an event-by-event basis reveals a detailed picture of the correlations between the ionization conditions and the ejection dynamics of the ionic fragments. The maximum KE of He⁺ is found to be governed by Coulomb repulsion from unscreened cations across all expansion regimes. The impact of ion-atom interactions resulting from the relatively low charge densities is increasingly relevant with less electron trapping. The findings are consistent with the emergence of a charged spherical shell around a quasineutral plasma core as the degree of ionization increases. The results demonstrate a complex relationship between measured ion KE and droplet ionization conditions that can only be disentangled through the use of coincident single-pulse TOF and scattering data.

1. Introduction:

X-ray free electron lasers (FELs) generate extremely intense, coherent, ultrashort pulses that have enabled single-pulse imaging of nanoscale systems, such as clusters, viruses and quantum vortices^{1–4}. Interpretation of these experiments often relies on the conjecture that the pulses are sufficiently short such that the x-rays diffract before destroying the sample due to extensive ionization. However, intense light—matter interactions lead to a host of complex physical processes, which can play an important role in interpretation of these experiments^{1,5}. Isolated and self-bound noble gas clusters are an excellent model system to study these processes via x-ray diffraction and the energetics of the ionization products⁶. Here, we study the charging and ion ejection dynamics in large helium nanodroplets irradiated by intense soft x-ray pulses, exploring the relationship between the degree of ionization, charge density, and maximum ion kinetic energies.

When an atomic cluster is exposed to an intense x-ray pulse, electrons are initially "outer ionized," i.e., electrons escape the cluster following photoionization^{7,8}. The evolution of the charging process during the continued x-ray – cluster interaction depends strongly on x-ray intensity and cluster size. In one extreme, all photoionization results in outer ionization and thus, all freed electrons escape the cluster. The charged cluster then expands via Coulomb explosion as a result of the repulsion between unscreened ions^{7,8}. In the other extreme, with sufficient x-ray intensity and cluster size, the collective Coulomb potential of the cations becomes deep enough, such that the kinetic energy of photoelectrons is insufficient to escape, i.e., outer ionization is frustrated. The subsequent photoionization events result in "inner ionization", i.e., the creation of quasi-free electrons that are trapped by the Coulomb potential of the charged cluster. Assuming a homogeneous charge distribution, the Coulomb potential is deepest near the

droplet center and becomes shallower toward the surface. Thus, electron trapping is expected to originate at the center of the droplet and to move outwards as ionization progresses. The result is a quasineutral plasma core, which grows to encompass more of the cluster as inner ionization proceeds⁹. The hot, trapped electrons thermalize with the ionic cores, and the quasineutral nanoplasma expands hydrodynamically.

In reality, the expansion of charged clusters may proceed by a combination of hydrodynamic expansion and Coulomb explosion, depending on the cluster size¹⁰, atomic species¹¹, and the intensity¹² and wavelength¹³ of the incident radiation¹⁴. While an extensive body of literature exists describing strong near-infrared (NIR) light- cluster interactions^{9,11,13,15}-¹⁷, x-ray- cluster interactions have only more recently been investigated, motivated by the availability of short, intense x-ray pulses provided by FELs. The evolution of large xenon clusters ($\sim 30\text{-}600 \text{ nm}$) exposed to FEL pulses (hv = 91 - 850 eV) with typical intensities of $\sim 10^{14}$ - 10^{16} W/cm² has been described in terms of hydrodynamic expansion and indicate that three-body recombination plays an important role in the nanoplasma dynamics^{4,18}. Other studies on smaller xenon and argon clusters, as well as Xe-Ar mixed clusters, indicate a more complex situation in which the outer shell of a cluster may undergo Coulomb explosion, while the core forms a quasineutral nanoplasma, followed by hydrodynamic expansion. 19-21 Theoretical calculations predict that Ar₉₂₃ clusters exposed to VUV (20 eV), XUV (38 eV), and soft x-ray (90eV) pulses with the same total energy deposition exhibit a smooth transition in expansion behavior⁸. It ranges from a Coulomb explosion for soft x-rays, to hydrodynamic expansion after VUV irradiation, while the XUV-induced dynamics fall in between the two limiting cases⁸.

Early experiments on charged clusters provided quantities, such as ion mass and/or electron energy spectra, accumulated over many pulses, and averaged over laser fluences and

cluster sizes. 9,11,15,17 Using ultrashort, intense light sources, measurements, such as ion TOF spectra, can be acquired on a shot-by-shot basis. Although, if only ion TOF spectra are acquired, the analysis still relies on average photon fluxes and cluster sizes. More detailed information can be obtained via coincidence measurements at X-FELs, in which both the TOF spectrum and the x-ray scattering pattern are collected for each registered event. These simultaneous measurements have previously been demonstrated on highly ionized Xe clusters in the hydrodynamic expansion regime.^{4,18} Here, we apply the same concept to study the transition between Coulomb explosion and hydrodynamic expansion regimes in more moderately ionized He nanodroplets. Helium atoms contain only two electrons, both in the 1s shell, and x-ray photon energies used in this work are well above both the single and double ionization potential (IP) of helium (24.6 eV and 79 eV, respectively ^{22,23}) and, thus, also far from any resonances. The resulting x-ray scattering patterns can be analyzed in a straightforward fashion using the Rayleigh-Gans approximation^{3,24,25} to determine the droplet size and the absolute single-pulse photon flux incident on the droplet. The validity of this approximation and the simplicity of the helium atom electronic structure enable an accurate determination of the incident photon flux and a relatively simple theoretical description of the charging process by photoionization, devoid of both high charge states and Auger cascades.

In this work, we monitor the interaction of single intense x-ray pulses (hv = 838 eV, $\sim 10^{11} \text{ photons/pulse}$) with individual large helium droplets (radius $R_0 = 78 - 578 \text{ nm}$) via coincident single-pulse coherent x-ray scattering and ion TOF spectroscopy. The unique event-by-event measurements provide detailed access to droplet charging and ion ejection dynamics across a large range of ionization regimes, from nominally pure Coulomb explosion conditions well into the quasineutral nanoplasma regime. Simultaneous measurements of the absorbed

number of photons, the droplet size, and the ion TOF spectrum for each event provides unprecedented detail on the degree of ionization and corresponding ion kinetic energy release of each individual droplet. Measurements span He_N droplet sizes between N \approx 10⁷ and 10¹⁰, and droplet charges between \sim 9×10⁻⁵ and \sim 3×10⁻³ e/atom. In terms of the dimensionless frustration parameter α (see below)⁸, ionization conditions cover a range of α = 0.23-44.

In all ionization regimes accessible in this experiment, the observed maximum ion kinetic energy (KE_{max}) values are consistent with a theoretical model in which the ion KEs are governed by a combination of Coulomb repulsion in the collective cluster potential from unscreened ions and ion-atom interactions during the expansion. In the predominantly Coulomb explosion regime (small α), screening by trapped electrons is negligible and unscreened charges are homogeneously distributed throughout the cluster. The resulting ion TOF spectra are heavily impacted by interactions of ions with neutral atoms during the expansion process, due to the relatively low overall charge density in this study. In the predominantly hydrodynamic expansion regime (large α), frustrated ionization is initiated at the droplet center and expands outward, leading to increased localization of unscreened charges near the surface of the nanoplasma with increasing α . In this regime, the fastest ions contained in the TOF spectra reflect predominantly on ions originating from the surface and their kinetic energies are well captured by a model of an expanding thin, charged spherical shell.

2. Experiment:

The experiment is conducted using the LAMP chamber at the AMO instrument of the Linac Coherent Light ²⁶Source (LCLS)^{26–28}. A schematic of the experiment is illustrated in Fig. 1. A beam of helium droplets is produced upon the expansion of 99.9999% purity liquid helium into vacuum through a 5 µm nozzle cooled to 5.8 K at a backing pressure of 20 bar. The

measured average He_N droplet size is $< N > \sim 2 \times 10^9$, which is very close to the expectation value of $< N > \sim 1 \times 10^9$ from previous measurements at same conditions.²⁹ The droplet beam is intersected by short x-ray pulses (\sim 65 fs FWHM, h ν = 838 eV) that are delivered at a 120 Hz repetition rate. The x-rays are focused using a pair of KB mirrors to a nominal 2.5 µm² spot size in the interaction region. Based on the LCLS operating parameters and previous beamline transmission measurements, average pulse fluxes on the order of $\sim 10^{16}$ W/cm² ($\sim 10^{23}$ photons/m²) are expected in the interaction region. As described in the following, the exact values for each x-ray-cluster interaction are determined from the single-pulse scattering patterns. Scattered x-ray photons are detected with a two-panel pnCCD detector, 710 mm downstream from the x-ray focus. The active regions of the detector panels are separated by a gap of 1.5 mm and each panel has a 4.4×1.8 mm² gap to let the primary x-ray beam pass through. The detector records small angle x-ray scattering patterns ($(q \sim 2 \times 10^{-3} - 2 \times 10^{-2} \text{ Å}^{-1})$). About the interaction region, an ion TOF spectrometer²⁶ is aligned perpendicular to both the helium droplet and x-ray beams, detecting cations produced upon x-ray absorption. A 10 mm × 1 mm slit aperture is mounted on the ion extraction electrode and aligned perpendicular to the FEL beam to suppress detection of ionized background gas outside the FEL focus. The aperture also provides more direct access to the KE distribution of ejected cations, as TOF averaging effects due to ion emission angular distributions are greatly reduced. X-ray diffraction images (Fig. 1b) and ion TOF spectra (Fig. 1c) are recorded in coincidence for each detectable scattering event from a single droplet.

3. Results

3.1. Individual droplet sizes and absolute on-target photon fluxes

Over 30 minutes of data acquisition, 47 scattering images with sufficient signal for postanalysis were recorded. A typical scattering pattern is shown in Fig. 1b. Quantitative analysis of
the single-pulse x-ray scattering patterns using the Rayleigh-Gans approximation for optically
thin targets^{3,24,25} provides direct access to both the size of individual droplets as well as the
photon fluxes interacting with them. For small angle scattering in the Rayleigh-Gans regime, the
ring spacing in scattering patterns such as in Fig. 1B can be approximated by $\Delta\Theta \approx \frac{\lambda}{2R_0}$, where λ is the x-ray wavelength, R_0 the droplet radius and $\Delta\Theta$ is the difference in scattering angles
between rings. Fits to an analytic expression for the diffraction intensity, as described in Gomez
et al.,³ are used to derive the droplet radius.²⁹ Based on the number density of liquid ⁴He at a
temperature of 0.4 K,³⁰ $n_{LHe} = 2.18 \times 10^{28}$ m⁻³, the number of atoms in the droplet, N, is
determined from the radius by $N = \frac{4}{3}\pi R_0^3 n_{LHe}$.³¹ While a fraction of droplets in the beam were
previously found to have spheroidal shapes due to centrifugal distortion,³² droplets studied here
have an average aspect ratio of 1.05 and, for the purpose of this work, are approximated as
spheres.

The flux F (photons/m²) of the x-ray pulse interacting with the droplet is obtained from the total number of scattered photons, which is given by

$$I_{total} = \frac{8\pi^3 R_0^4 |n-1|^2}{\lambda^2} F \tag{1}$$

where *n* is the complex refractive index of liquid helium, $n = 1-4.32 \times 10^{-5} + 1.75 \times 10^{-7}i$. ^{3,33}

The value of n is obtained from the atomic scattering factors for He atoms³⁴ of $f_1^0 = 2.02$ and $f_2^0 = 8.16 \times 10^{-3}$ at 838 eV ($\lambda = 1.5$ nm), the number density of liquid helium of n_{LHe} , and the classical electron radius $r_e = 2.818 \times 10^{-15}$ m according to³³:

$$n = 1 - \frac{n_{LHe} r_e \lambda^2 (f_1^0 - i f_2^0)}{2\pi}$$
 (2)

The value of I_{total} is obtained by scaling the total scattering intensity from a droplet with radius R_0 to the range of observable scattering vectors, which excludes the central hole in the detector and the gap between the CCD plates. The scattered intensity is expressed in photon units using the calibrated detector single photon response.

The number of absorbed photons is obtained as³³:

$$N_{abs} = 2r_e \lambda \times f_2^0 \frac{4\pi R_0^3}{3} n_{LHe} F \tag{3}$$

In this work, droplet radii range from R_0 =78 nm – 578 nm, and the photon flux ranges from F=1.3×10²¹ to 5.7×10²² photons/m². The droplet radius is determined within ~5% and the photon flux is accurate within ~20% with the uncertainty arising from using a nominal ADU/photon ratio, the initial detector noise subtraction and using spherical droplet approximation. The variation in photon flux mostly results from the spatial distribution of the detected droplets with respect to the FEL beam axis. Some additional variation originates from the pulse-to-pulse intensity fluctuations of the FEL.

At a photon energy of 838 eV, photoabsorption leads to photoionization with the number of absorption events given by Eq. (3). We neglect single-photon double ionization events in these estimates, since the relative cross section for double vs. single ionization at 838 eV photon energy is less than 3%.²³ As such, the number of ions resulting from photoionization, N_{ion} , is equal to N_{abs} . Note that N_{ion} does not necessarily correspond to the number of electrons leaving the droplet. Additionally, N_{ion} does not include ions resulting from secondary ionization.

3.2. Helium cation TOF spectra

Cation TOF spectra provide information about the relative abundance of different cation species produced in the x- ray – cluster interaction, as well as the ion kinetic energies. An example cation cluster spectrum is shown in Fig 1c. The leftmost (i.e., shortest TOF) feature

corresponds to the singly charged He⁺ atomic ions, with the features following at longer times of flight corresponding to He_n⁺ clusters with n>1. Numerical ion trajectory simulations (SIMION®) are used to convert from TOF to initial ion kinetic energy in the interaction region. The analysis is focused on the short-TOF edge of the peaks, corresponding to the maximum ion kinetic energy, since many peaks exhibit strong saturation effects at longer TOF. Additionally, the particular layout and operating voltages of the TOF spectrometer leads to the unusual situation where almost all ions with nonzero initial kinetic energy, independent of their emission direction, arrive at the detector before the zero kinetic energy ions. Even most ions originally ejected away from the detector are accelerated such that they overtake the zero kinetic energy ions in the drift region of the spectrometer and their TOF signals overlap with ions emitted toward the detector. Thus, the recorded TOF spectra were calibrated by using the maximum TOFs of the He_n^+ , n=1,2,...,8 signals to identify the KE=0 positions of the different mass peaks. The precision of this method was maximized by using the weakest intensity hits that contained the required mass peaks, which circumvents potential issues with signal modulations at the long-TOF peak edges in the more intense hits caused by electronic ringing. Due to the overlap of signals from ions ejected both toward and away from the detector, it is rather challenging to recover the complete ion kinetic energy distribution from the TOF signals. However, ions ejected toward the detector with the highest kinetic energies are always the first to arrive at the detector. Therefore, KE_{max} can be faithfully recovered from the shortest TOF. Uncertainty in determining KE_{max} arising from electronic signal noise dominates for weaker hits (and correspondingly for ion features with smaller KE_{max}). Systematic errors arising from the limited precision in locating the interaction region with respect to the center of the ion TOF spectrometer dominate for strong hits and higher KE_{max} . In particular, for He^+ , which will be the focus of the discussion, the

smallest KE_{max} are determined within 20% and the largest within 6% uncertainty. KE_{max} are determined for He^+ , as well as He_2^+ , He_3^+ and He_4^+ when present. For example, the KE_{max} corresponding to the TOF spectrum in Fig. 1c are 103, 123, 24, and 8 eV, respectively, for the four ion species.

The trajectory simulation is also used to estimate the transmission of the TOF spectrometer. To estimate the noise threshold, we use the integrated signal of non-saturated TOF spectra, the calculated yield of generated ions $N_{\rm ion}$, and the simulated spectrometer transmission function. The detection threshold of the measurement is estimated to be on the order of ~10's of ions per TOF channel.

3.3. Size- and Charge-Dependent TOF spectra

Fig. 2 illustrates some of the information revealed by the coincidence measurements of single-pulse TOF spectra and scattering images. The ion TOF spectra in Fig. 2 are grouped into four panels according to the droplet size (horizontal axis). Panels a, b, c, d correspond to droplets consisting of $\sim 10^7$, $\sim 10^8$, $\sim 10^9$ and $\sim 10^{10}$ atoms, respectively. The respective color codes of black, blue, green, and red, are also used in Fig. 3-6 to identify droplet sizes associated with the data points. In each panel, the TOF spectra have an offset corresponding to the number of ionization events per atom of the droplet, N_{ion}/N (vertical axis). In each spectrum, the peak with the smallest TOF ($\sim 2~\mu$ s) corresponds to He⁺ ions, followed by He_n⁺ fragments with n=2,3,4... with increasing TOF.

Several trends are readily apparent in Fig. 2. As the droplet size increases for a given average charge per atom (i.e., for constant photon flux), the corresponding TOF spectra extend to increasingly larger helium cation clusters. For example, for $N_{ion}/N \approx 2-3 \times 10^{-4}$, the largest detected He_n⁺ cluster size increases from n=3 for $N\sim10^7$ to n=8 for $N\sim10^{10}$. Conversely,

within a given size regime, the He_n^+ size distribution shifts from larger to smaller values of n with increasing average charge. In particular, at $N_{ion}/N \gtrsim 1.8 \times 10^{-3}$ e/atom no $\text{He}_{n\geq 3}^+$ features are observed whereas the monomer peak becomes the most intense spectral feature for all droplet sizes. Additionally, a further increase in N_{ion}/N leads to a broadening of the $\text{He}_{n=1,2}^+$ peaks towards shorter times of flight, corresponding to an increase in the ion kinetic energy. Note that we do not observe any signatures of He^{++} fragments in the TOF spectra.

4. Analysis

4.1. Cluster charging and degree of frustrated ionization

As an intense x-ray pulse passes through the target, the series of ionization events leads to a concomitant increase of the collective Coulomb potential of all ions in the droplet. Assuming a homogeneous distribution of ionization events, ¹⁴ the Coulomb potential experienced by an electron can be described by

$$V_{Coul} = \begin{cases} -\frac{e}{4\pi\varepsilon_0} \frac{N_{eff}}{2R_0} \left(3 - \frac{r^2}{R_0^2} \right), & r < R_0 \\ -\frac{e}{4\pi\varepsilon_0} \frac{N_{eff}}{r} & , & r \ge R_0 \end{cases}$$
 (4)

Here, e is the elementary charge, ε_0 is the permittivity of free space, and r corresponds to the distance from the droplet's center. N_{eff} is the net number of charges contributing to the Coulomb potential as described in the following. According to Eq. (4), the kinetic energy of the primary photoelectrons, $E_{kin}(e^-)=hv-IP \lesssim 813.4 \text{ eV}$ (IP: atomic ionization potential), will be insufficient to overcome the Coulomb potential if the droplet's charge reaches a critical value. At this point, the locally freed electrons will be trapped as quasi-free electrons and begin to form a nanoplasma. The potential in Eq. (4) is deepest at r=0. Thus, frustration of ionization is expected to

commence at the droplet center and expand outward with increasing degree of ionization during the passage of a sufficiently intense x-ray pulse through the target. With the onset of photoelectron trapping, the effective number of ions contributing to the Coulomb potential, i.e., the net droplet charge, is smaller than the total number of created ions, $N_{eff} < N_{ion}$, due to partial screening of the ionic background by trapped electrons. Note that the term for $r < R_0$ in Eq. (4) is nominally only valid for conditions before the onset of frustration, as trapped electrons will move towards the center of the charged droplet and therefore the net charge distribution is no longer homogeneous.¹⁴ In addition, this discussion neglects any secondary ionization events.

The degree of ionization frustration is quantified by the dimensionless frustration parameter⁸

$$\alpha = \frac{N_{ion}}{N_{frust}},\tag{5}$$

whereby N_{frust} is the effective number of droplet charges needed to completely frustrate outer ionization across the entire droplet. N_{frust} can be determined by equating the maximum kinetic energy $E_{kin}(e^{-}) = 813.4 \text{ eV}$ of an electron to its Coulomb energy at the surface of a cluster with radius R_0 , according to Eq. (4) leading to

$$N_{frust} = \frac{4\pi\varepsilon_0}{e^2} E_{kin}(e^-) R_0 \approx 565 \cdot R_0(nm) . \tag{6}$$

From eqs. (4)-(6) it follows that frustrated ionization sets in for $\alpha = 2/3$ and full frustration is reached at $\alpha \gtrsim 1$, after which all additional photon absorption leads to inner ionization. Note that α needs to be somewhat larger than 1 to reach full frustration as electron trapping from the core outwards leads to partial screening of ions and thus, not all N_{ion} ions created by photoionization contribute to the droplet charge, with the exact value depending on the conditions of the given system. The degree of frustration has direct impact on the droplet

expansion dynamics following ionization, with Coulomb explosion dominating for $\alpha \lesssim 1$ and hydrodynamic expansion of the nanoplasma for $\alpha \gg 1$. At intermediate values with α on the order of ~10, the expansion does not clearly fall into either of these limiting categories. We emphasize that the frustration parameter is based on the number of electrons produced in photoionization alone. Taking into account the secondary electron impact ionization, the number of produced ions may be larger by up to a factor of ~30, based on the ratio between the photon energy and the He atom IP. However, with increasing charge density and the emergence of lower KE electrons, there is also an increased likelihood of electron-ion recombination. As such, the total number of ions evolves with time in a complex fashion that is beyond the scope of this work. We therefore resort to define the frustration parameter based on the primary photoionization alone.

From $N_{ion} \propto FR_0^3$ it follows that $\alpha \propto FR_0^2$, elucidating the relationship between x-ray flux, droplet size, and expansion regime. Note, in particular, that both the x-ray flux and the droplet size contribute independently to the degree of ionization frustration. Thus, both need to be determined on an event-by-event basis in order to evaluate the regime of ionization for every x-ray-droplet interaction. The results presented herein are associated with frustration parameters between $\alpha = 0.23$ and $\alpha = 44$, spanning the entire range from pure Coulomb explosion to significant ionization frustration, expected to lead predominantly to hydrodynamic expansion.

4.2. Relation between maximum kinetic energy release and degree of frustration

Different cluster disintegration mechanisms typically give rise to different kinetic energies of the ions. ^{15,35,36} Thus, it is instructive to plot the maximum detected ion kinetic energy KE_{max} against the frustration parameter α. This relation is shown for He⁺, He₂⁺, He₃⁺ and He₄⁺ ions in Fig. 3 a, b, c, and d, respectively. For monomer and dimer cations, a clear trend emerges,

whereby KE_{max} increases continuously with increasing α for $\alpha \lesssim 20$ and appears to saturate for larger degrees of frustration. For trimers and tetramers, no clear trend emerges. However, the characteristic kinetic energies decrease with increasing size n of the He_n⁺ fragments.

In the following discussion, we will use the results for He⁺ ions in Fig. 3a to derive a quantitative model for explaining the observed kinetic energy dependences based on Coulomb repulsion and ion-atom scattering effects. Results for He_n⁺ clusters are not included in the discussion. Such clusters are formed upon attachment of one or more He atoms to He⁺ ions, with some unknown dynamics, the study of which is beyond the scope of this work.

5. Discussion

Fig. 3a indicates a close relationship between the degree of frustration reached during the x-ray – cluster interaction and the maximum kinetic energy of ejected He⁺ ions. The physical origin of the observed trend, however, is not readily apparent and requires additional analysis and modeling. Both Coulomb explosion and hydrodynamic expansion may contribute to ion kinetic energy distributions across the range of α values studied here. KE_{max} , however, is expected to be defined by Coulomb repulsion effects, as indicated by the following estimates. The average ion kinetic energy in a hydrodynamic expansion is described by³⁷

$$\langle KE_{hyd} \rangle = \frac{3}{2} k_b T_e \frac{N_{ion}}{N},\tag{7}$$

where N_{ion}/N is the average charge state per atom, k_b is the Boltzmann constant, and T_e is the initial electron temperature of the nanoplasma. N_{ion}/N is derived from the scattering images as described above, and the remainder of the right-hand term in Eq. (7) is estimated by the kinetic energy of the trapped photoelectrons: $\frac{3}{2}k_bT_e \simeq 813.4 \ eV$. With N_{ion}/N varying between $\sim 9\times 10^{-5}$ and $\sim 3\times 10^{-3}$, $\langle KE_{hyd}\rangle$ ranges from $\sim 0.07-3$ eV. These values are ~ 2 orders of magnitude smaller than the observed KE_{max} (Fig. 3). The inclusion of electron impact ionization would

bring $\langle KE_{hyd} \rangle$ at most to within one order of magnitude of KE_{max} . Thus, we proceed by comparing KE_{max} to the Coulomb potential energy experienced by an ion at the surface of the charged droplet.

5.1. Surface Coulomb Potential Energy

The potential energy of an ion at the droplet's surface $(r = R_0)$ is $U_{Coul}(r = R_0) = \frac{e^2}{4\pi\epsilon_0} \frac{N_{eff}}{R_0}$, taking into account the screening of ions by trapped electrons. The effective number of unscreened charges, N_{eff} , contributing to the Coulomb potential is approximated by the difference between the total number of ions and the number of trapped electrons: $N_{eff} = N_{ion} - N_{trap}$. The underlying assumption is that, on average, each trapped electron screens one cationic charge. N_{eff} is estimated for three distinct frustration regimes: (i) $\alpha < 0.67$, (ii) $0.67 \le \alpha \le 2.5$, and (iii) $\alpha \ge 2.5$.

- (i) For α < 0.67, the Coulomb potential according to Eq. (4) is insufficient for electron trapping throughout the entire droplet. Thus, the number of unscreened charges is equivalent to the total number of ions, i.e., $N_{eff} = N_{ion}$.
- (ii) The range $0.67 \le \alpha \le 2.5$ corresponds to partial frustration, in which electron trapping is achieved within a radius, $0 < r_{frust} < R_0$, as governed by the potential in Eq (4). A finite step simulation is implemented, as described in the Supporting Information (SI), to determine the number of trapped electrons, N_{trap} , in this regime. N_{eff} is then estimated as $N_{eff} = N_{ion} N_{trap}$.
- (iii) For $\alpha \gtrsim 2.5$, full frustration is achieved at time t_f , with r_{frust} (t_f) = R_0 . All additional ionization at times $t > t_f$ is subject to electron trapping and does not contribute to the effective number of charges. Thus, N_{eff} can be estimated by $N_{eff} = N_{frust}$.

Fig. 4 shows the ratio of the measured KE_{max} and the surface Coulomb potential energy, U_{Coul} , based on the effective number of unscreened charges N_{eff} as described above. The color codes of the data points indicate the same size regimes as in Fig. 2,3. A continuous trend emerges, in which the KE_{max} is always smaller than the Coulomb energy of a He⁺ ion at the outermost cluster surface ($r = R_0$), and KE_{max} / U_{Coul} varies between ~ 0.03 and ~ 0.4 across different frustration regimes. The similarities in Fig. 3a and Fig. 4 arises from the fact that the surface potential is constant for $\alpha \gtrsim 2.5$.

5.2. KE_{max} in the highly frustrated regime

As shown by Fig. 4, as α exceeds ~20, KE_{max}/U_{Coul} begins to plateau, approaching a ratio of ~0.4. In this highly frustrated regime, due to substantial electron trapping, unscreened ions occupy less than 4 nm (see 5.4 and S.I.) of the outermost shell of the charged droplet, with the remainder of the droplet comprising of a quasineutral core. The range of radii corresponds to less than 2% of the droplet radius. As such, we model the ion ejection in this regime as the expulsion of a thin spherical shell of N_{eff} unscreened ions. Within this model, the average ion kinetic energy KE_{shell} corresponds to the stored energy per ion of a spherical shell:

$$KE_{shell} = E_{shell}/N_{eff} = \frac{1}{2} \frac{e^2}{4\pi\epsilon_0} \frac{N_{eff}}{R_0} = \frac{1}{2} U_{coul}.$$
 (8)

The ratio of 1/2 between the average KE per ion and the Coulomb potential is very close to the observed value of ~0.4 in the highly frustrated regime, supporting the picture that a thin spherical shell expansion captures the dominant physics for $\alpha \gtrsim 20$.

5.3. KE_{max} in the weakly frustrated regime

The expected maximum ion KE for a Coulomb explosion of a homogeneously charged sphere is equivalent to U_{Coul} . However, for $\alpha < 20$, the measured maximum ion kinetic energies are significantly smaller, with KE_{max}/U_{Coul} reaching values as small as ~1/30 in the non-

frustrated regime, where pure Coulomb explosion is expected (Fig. 4). We propose that this, at first glance, counterintuitive trend is the result of ion-atom interactions throughout the expansion process. Due to the relatively low charge densities herein, ionization of the droplets initiates a Coulomb explosion of unscreened ions within a dense medium of neutral atoms. Ion-atom interactions within the charged droplet impart energy on the neutral atoms and, thus, the expansion will likely be marked by a more collective motion of neutral atoms and ions than in the highly frustrated regime. While a detailed modeling of this motion is beyond the scope of this work, it is instructive to analyze the ratio of the observed KE_{max} and the surface Coulomb potential U_{Coul} within a picture of a number of (hypothetical) ion-neutral collisions that would be required for ions with initial kinetic energy of U_{Coul} to decelerate to the observed KE_{max} .[38]

We treat ion-atom collisions within a hard spheres model with equal mass and size of the collision partners, He⁺ and He. The average He⁺ kinetic energy loss per collision is estimated by assuming elastic collisions of an ion with a He atom at rest. With the probability of a given impact parameter scaling linearly with impact parameter³⁹, averaging over all collision geometries yields a mean kinetic energy loss per collision of 50%.

Upon undergoing m collisions the ion kinetic energy, KE_m^{th} , is:

$$KE_m^{th} = U_{Coul} \cdot 0.5^m \,. \tag{9}$$

By equating KE_m^{th} with the measured values KE_{max} , the minimum number of collisions can be estimated, as is plotted in Fig. 5. We observe a decrease in the minimum number of collisions, with a continuous trend that ranges from $m \gtrsim 5$ at small α to $m \gtrsim 1.5$ as we approach $\alpha \sim 20$. This

decrease in number collisions correlates with the increasing plasma core, as frustration parameter increases.

5.4 Illustration of Droplet Charge Distributions

Fig. 6 shows the ratio of the thickness δ_{shell} of the shell of unscreened ions and the droplet radius R_0 as a function of the degree of frustration in semilogarithmic scale. The insets provide visualizations of three specific cases corresponding to (i) the limit of no frustration / pure Coulomb explosion, (ii) the onset of full frustration, and (iii) the highest degree of frustration detected in the experiment. In the insets, screened and unscreened ions are depicted as light and dark blue spheres, respectively, and neutral helium atoms are depicted as yellow. The smoothness of the curve in Fig. 6 attests to the fact that it is a theoretical estimate as described below, whereby the experimental data points define the alpha values at which it is evaluated.

The thickness of the shell of unscreened ions, δ_{shell} , is calculated from the number of unscreened ions, N_{eff} , from section 5.1, and the overall cation charge density $\rho_{He^+} = N_{ion}/\frac{4}{3}\pi R_0^3$ and assuming a sharp boundary between the screened and unscreened ions. The shell thickness, δ_{shell} , is related to N_{eff} and ρ_{He^+} using the following equation:

$$N_{eff} = \frac{4}{3}\pi [R_0^3 - (R_0 - \delta_{shell})^3] \rho_{He^+}$$
 (10),

For the smallest values of α , no electron trapping occurs, and unscreened ions are distributed homogeneously throughout the cluster ($\delta_{shell} = R_0$). However, once frustration sets in, the normalized shell thickness, δ_{shell} / R_0 , decreases rapidly from 1 to 0.15 over the range $0.67 < \alpha \le 2.5$, corresponding to the transition from no to full frustration. The normalized shell thickness continues to decrease with increasing frustration, reaching a mere 0.8% of the droplet radius at $\alpha = 44$. We note that for $\alpha > 20$, the absolute shell thickness saturates at ~ 3 nm (see S.I.). This region corresponds to the plateau observed in the α -dependence of KE_{max} in Fig. 3a.

Taking into account that the Coulomb potential at the cluster surface already saturates for much smaller values of $\alpha \approx 2.5$, the "delayed" saturation of KE_{max} in Fig. 3a and the correspondence of the plateau regions for the KE_{max} and the absolute thickness of the unscreened ion shell lends further support to the concept that both Coulomb repulsion and ion-atom interactions play important roles for determining the maximum ion KEs.

The clusters studied here in a single experiment, under nominally identical experimental conditions, cover the entire range of charging conditions, from a homogeneous distribution of ions subject to mutual Coulomb repulsion to quasineutral nanoplasmas extending across >99% of the droplet diameter. Differentiating these charged cluster varieties has only become possible through the single-pulse measurement capabilities developed at X-FELs. At the same time, they illustrate the importance of complete characterizations of light-matter interactions on a pulse-by-pulse basis in order to understand the underlying physics.

6. Conclusions:

Charging and disintegration of helium nanodroplets exposed to intense soft x-ray pulses is studied by single pulse coincident ion TOF spectroscopy and small-angle x-ray scattering. Experimental conditions span from pure Coulomb explosion to a regime of deeply frustrated ionization. The low ion density due to the small x-ray absorption cross section of He leads to a complex relationship between measured ion kinetic energies and cluster ionization conditions that can only be disentangled through the coincident single-pulse measurement capability. Maximum ion kinetic energies are modeled by a combination of Coulomb repulsion from unscreened cluster ions and ion-atom interactions during the expansion. We find that the measured kinetic energies reflect on ions created deeper inside the droplet in the Coulomb explosion limit and on ions originating from the surface in the deeply frustrated, hydrodynamic

limit. The results demonstrate the need for quantitative single pulse information to derive physical insight from interpreting ion TOF spectra in intense x-ray—cluster interactions.

Acknowledgments:

This work was supported by the Atomic, Molecular, and Optical Sciences Program of the US Department of Energy, Office of Science, Office of Basic Energy Sciences, Chemical Sciences, Geosciences and Biosciences Division, through Contract No. DE-AC02-05CH11231 (C.A.S., M.P.Z., C.Ba., A.S.C., O.G.) and Contract No DE-AC02-06CH11357 (MB, C.Bo.). A.J.F., C.J., and A.F.V. were supported by the National Science Foundation under Grants No. CHE-1664990 and DMR-1701077. C.Bo. acknowledges the Swiss National Science Foundation via the National Center of Competence in Research – Molecular Ultrafast Science and Technology NCCR - MUST. Portions of this research were carried out at the LCLS, a national user facility operated by Stanford University on behalf of the U.S. DOE, OBES under beam-time Grant No. LA1214: Time-Resolved Imaging of X-ray Induced Dynamics in Clusters. Use of the Linac Coherent Light Source (LCLS), SLAC National Accelerator Laboratory, is supported by the U.S. Department of Energy, Office of Science, Office of Basic Energy Sciences under Contract No. DE-AC02-76SF00515.

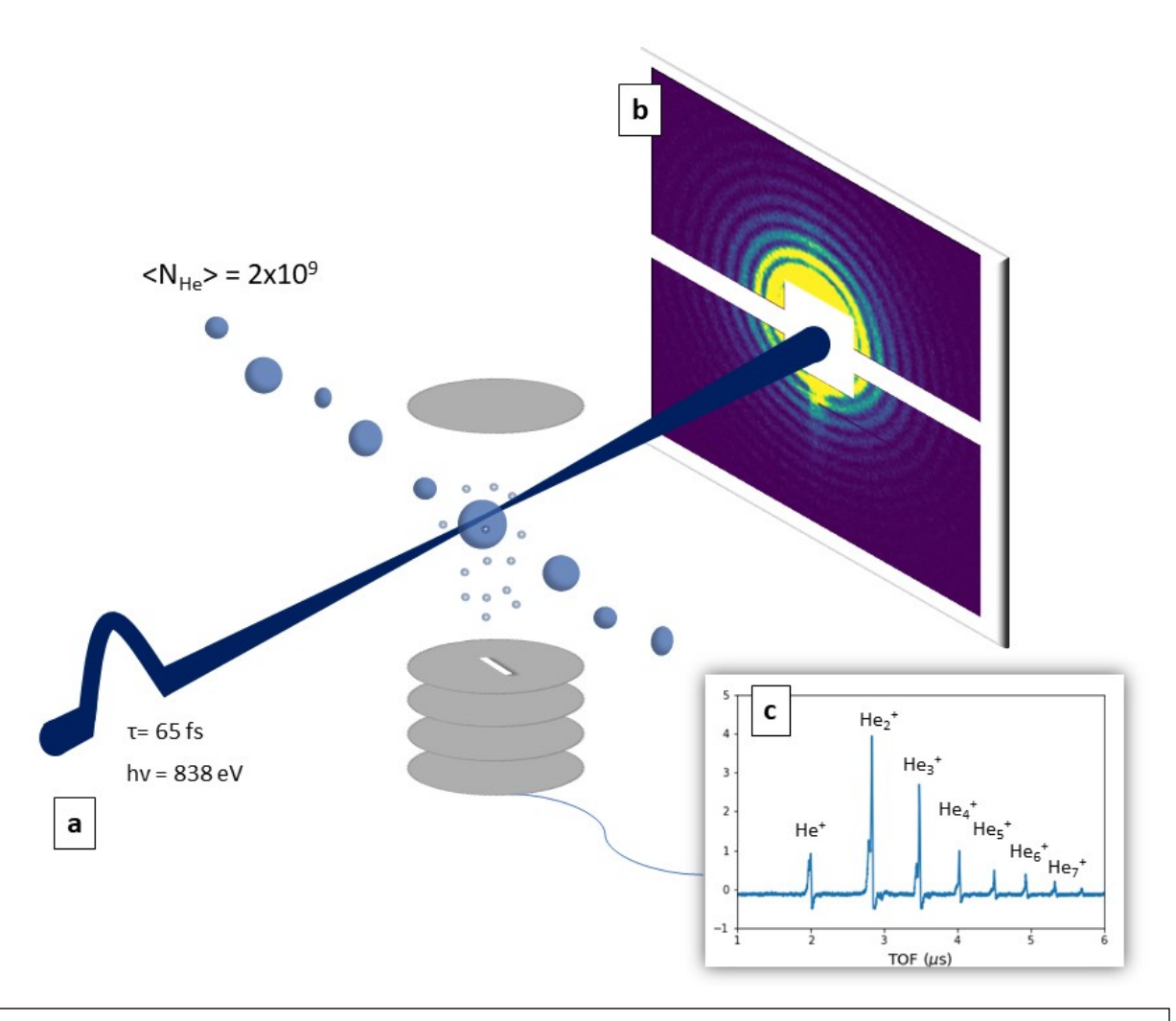


Figure 1. a) Diagram of experimental setup. b) Sample diffraction image. c) Coincident ion TOF spectrum.

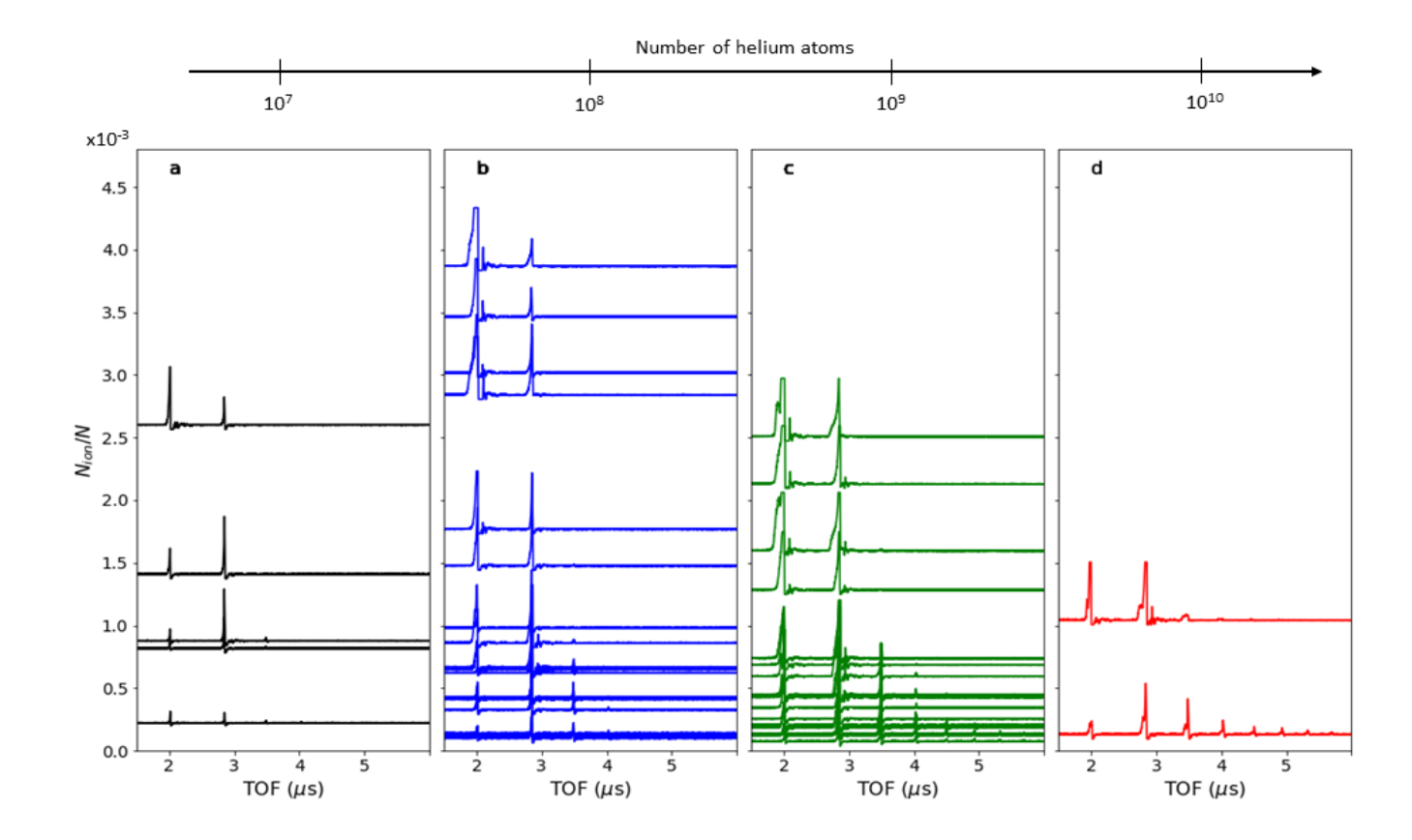


Figure 2. Helium droplet ion TOF spectra are vertically sorted by the number of photogenerated ions, normalized to the number of helium atoms. Panels a-d feature TOF spectra obtained in droplets of different sizes ($\sim 10^7$, 10^8 , 10^9 and 10^{10} atoms). The size regimes are further indicated by the colors of the TOF spectra, and the same color code is used in all subsequent figures.

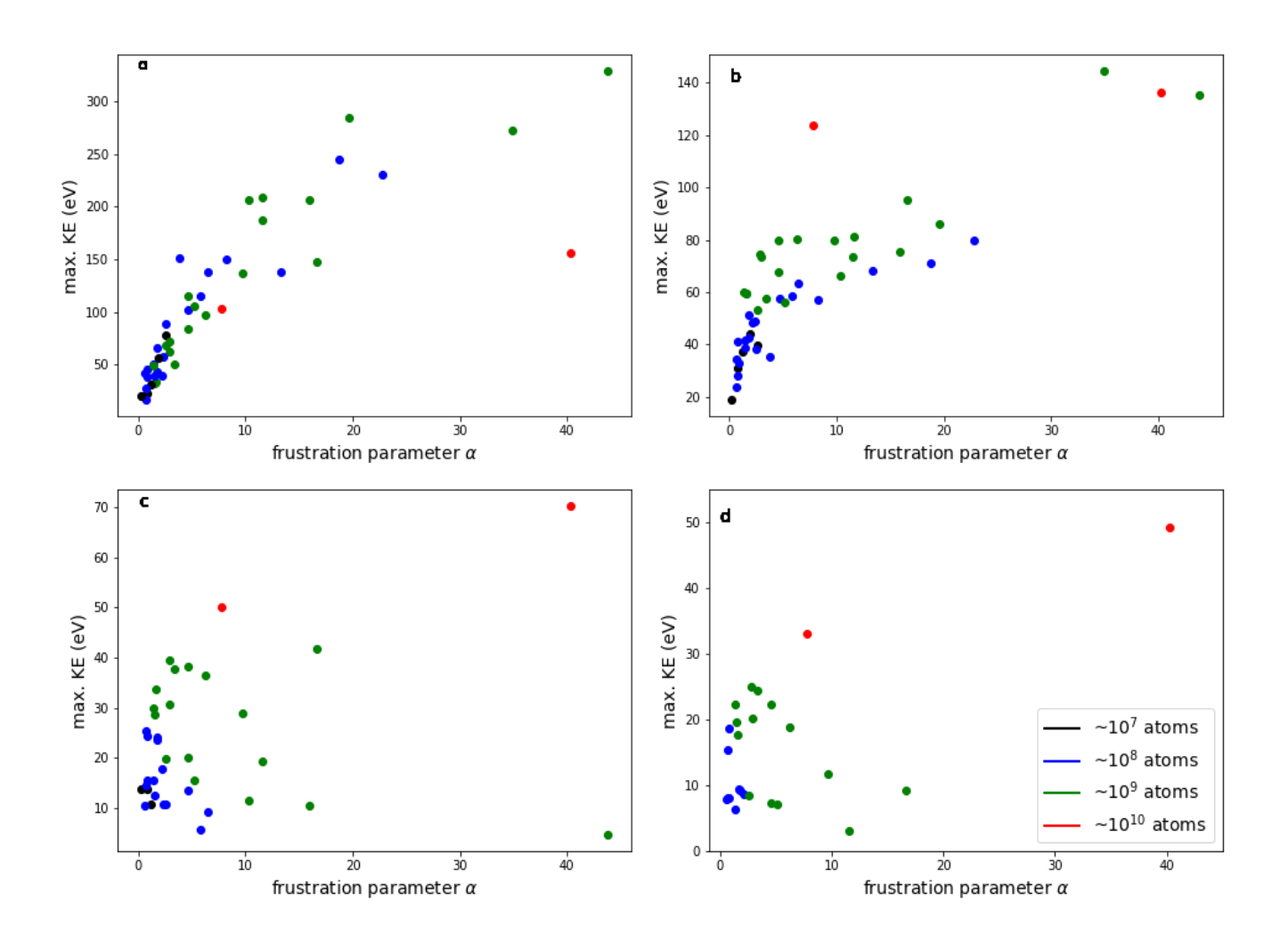


Figure 3. Maximum ion kinetic energies derived from the shortest flight times in the ion TOF spectra and plotted as a function of the frustration parameter α for a) monomer, b) dimer, c) trimer, and d) tetramer cations

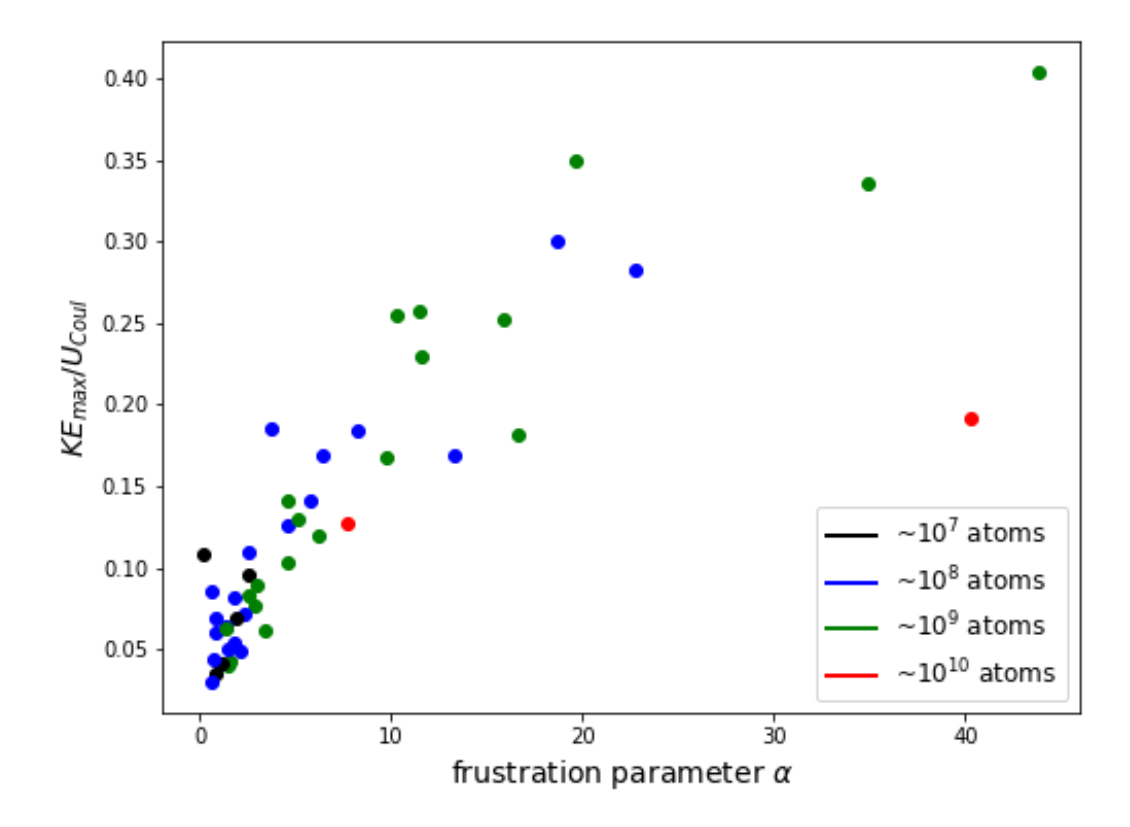


Figure 4. Ratio of the maximum He⁺ kinetic energy and the Coulomb energy of singly charged ions at the droplet surface.

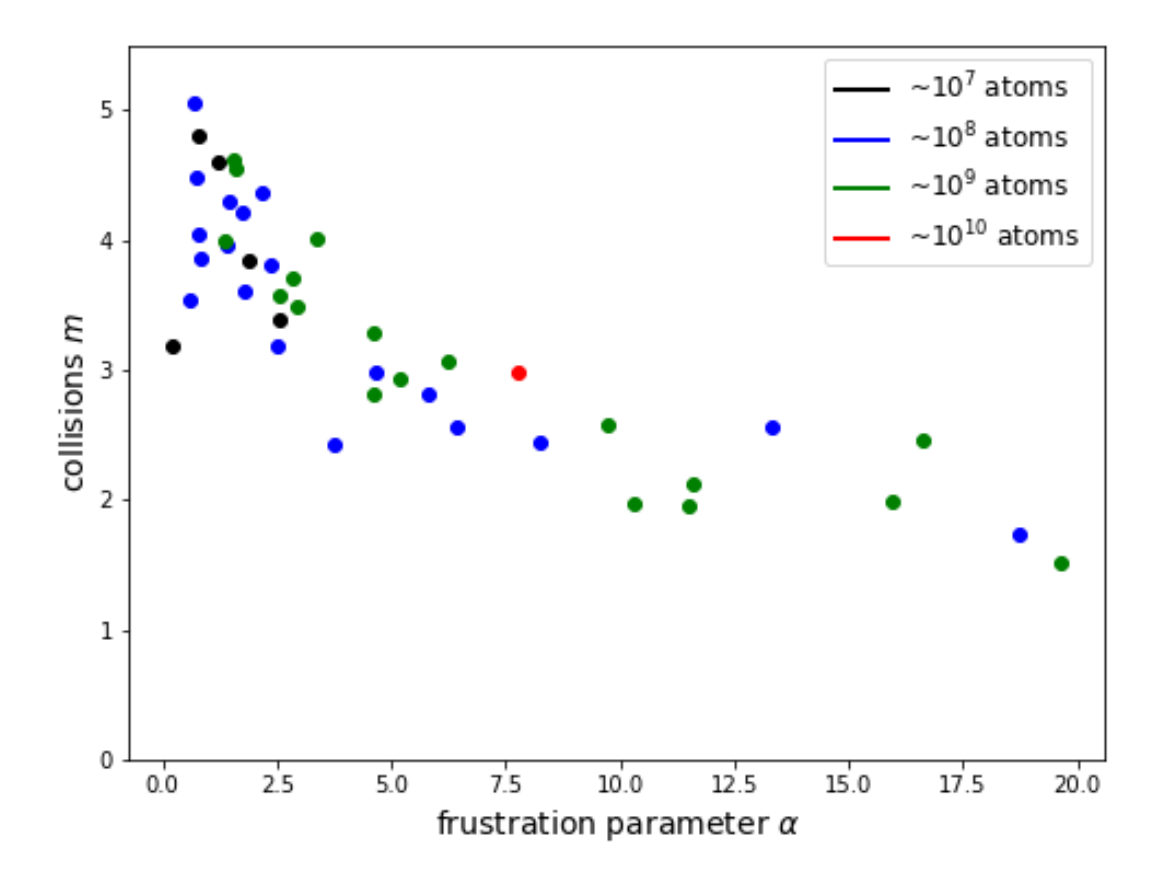


Figure 5. Minimum number of ion-atom collisions required to decelerate the ion from the value of the Coulomb energy at the cluster surface to the measured maximum kinetic energy.

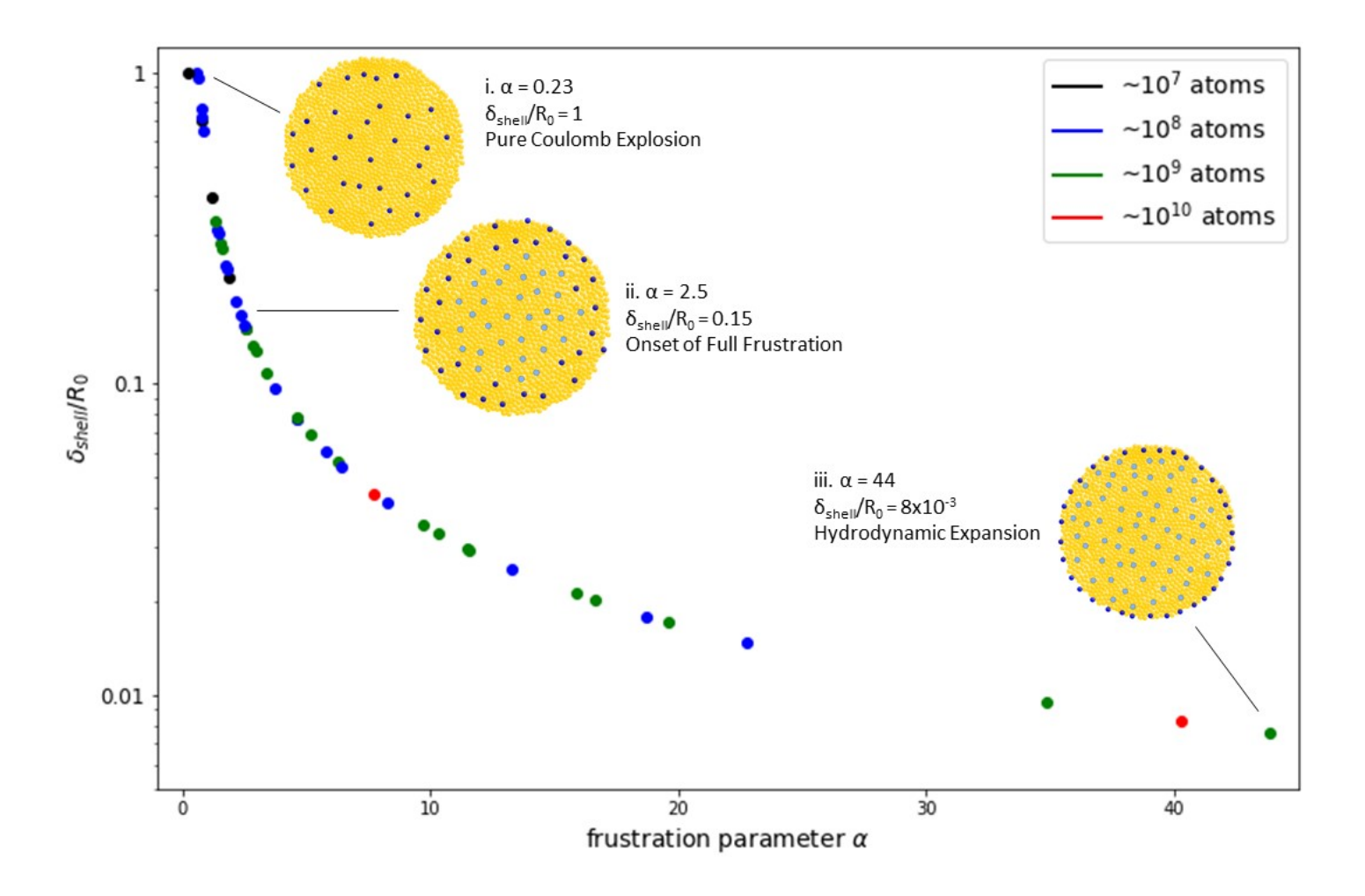


Figure 6. Thickness of the shell of unscreened ions normalized to the droplet radius versus the frustration parameter. Pictograms indicate the structure of the charged droplets, which are modeled by charged shells of unscreened ions (dark blue) surrounding a quasineutral plasma core (light blue), interspersed amongst neutral helium atoms (yellow). The three illustrations correspond to different ionization/expansion regimes: (i) no frustration, (ii) onset of full frustration, and (iii) highest observed degree of frustration.

References:

- 1. Bostedt, C. *et al.* Ultrafast x-ray scattering of xenon nanoparticles: Imaging transient states of matter. *Phys. Rev. Lett.* **108**, 1–5 (2012).
- 2. Seibert, M. M. *et al.* Single mimivirus particles intercepted and imaged with an X-ray laser. *Nature* **470**, 78–82 (2011).
- 3. Gomez, L. F. *et al.* Shapes and vorticities of superfluid helium nanodroplets. *Science* (80-.). **345**, 906–909 (2014).
- 4. Gorkhover, T. *et al.* Nanoplasma dynamics of single large xenon clusters irradiated with superintense X-ray pulses from the linac coherent light source free-electron laser. *Phys. Rev. Lett.* **108**, 1–5 (2012).
- 5. Ho, P. J. *et al.* The role of transient resonances for ultra-fast imaging of single sucrose nanoclusters. *Nat. Commun.* **11**, 1–9 (2020).
- 6. Rupp, D. *et al.* Imaging plasma formation in isolated nanoparticles with ultrafast resonant scattering. *Struct. Dyn.* **7**, (2020).
- 7. Bostedt, C. *et al.* Multistep ionization of argon clusters in intense femtosecond extreme ultraviolet pulses. *Phys. Rev. Lett.* **100**, 1–4 (2008).
- 8. Arbeiter, M. & Fennel, T. Rare-gas clusters in intense VUV, XUV and soft x-ray pulses: Signatures of the transition from nanoplasma-driven cluster expansion to Coulomb explosion in ion and electron spectra. *New J. Phys.* **13**, 1–13 (2011).
- 9. Ditmire, T., Donnelly, T., Rubenchik, A., Falcone, R. & Perry, M. Interaction of intense laser pulses with atomic clusters. *Phys. Rev. A* **53**, 3379–3402 (1996).
- 10. Schorb, S. *et al.* Size-dependent ultrafast ionization dynamics of nanoscale samples in intense femtosecond x-ray free-electron-laser pulses. *Phys. Rev. Lett.* **108**, 1–5 (2012).
- 11. Lezius, M. *et al.* Explosion Dynamics of Rare Gas Clusters in Strong Laser Fields. *Phys. Rev. Lett.* **80**, 261–264 (1998).
- 12. Arbeiter, M. & Fennel, T. Ionization heating in rare-gas clusters under intense XUV laser pulses. *Phys. Rev. A* **82**, 1–7 (2010).
- 13. Saalmann, U., Siedschlag, C. & Rost, J. M. Mechanisms of cluster ionization in strong laser pulses. *J. Phys. B At. Mol. Opt. Phys.* **39**, R39–R77 (2006).
- 14. Saalmann, U. Cluster nanoplasmas in strong FLASH pulses: formation, excitation and relaxation. *J. Phys. B At. Mol. Opt. Phys.* **43**, 1–8 (2010).
- 15. Ditmire, T. *et al.* High energy Ion explosion of atomic clusters: Transition from molecular to plasma behavior. *Phys. Rev. Lett.* **78**, 2732–2735 (1997).
- 16. Fennel, T. *et al.* Laser-driven nonlinear cluster dynamics. *Rev. Mod. Phys.* **82**, 1793–1842 (2010).

- 17. Ditmire, T. *et al.* High-energy ions produced in explosions of superheated atomic clusters. *Lett. to Nat.* **386**, 54–56 (1997).
- 18. Rupp, D. *et al.* Recombination-Enhanced Surface Expansion of Clusters in Intense Soft X-Ray Laser Pulses. *Phys. Rev. Lett.* **117**, 1–6 (2016).
- 19. Thomas, H. *et al.* Explosions of xenon clusters in ultraintense femtosecond X-ray pulses from the LCLS free electron laser. *Phys. Rev. Lett.* **108**, 1–5 (2012).
- 20. Hoener, M. *et al.* Charge recombination in soft x-ray laser produced nanoplasmas. *J. Phys. B At. Mol. Opt. Phys.* **41**, 1–5 (2008).
- 21. Thomas, H. *et al.* Shell explosion and core expansion of xenon clusters irradiated with intense femtosecond soft x-ray pulses. *J. Phys. B At. Mol. Opt. Phys.* **42**, 1–7 (2009).
- 22. Madden, R. P. & Codling, K. New autoionizing atomic energy levels in He, Ne, and Ar. *Phys. Rev. Lett.* **10**, 516–518 (1963).
- 23. Samson, J. A. R. *et al.* Double photoionization of helium. *Phys. Rev. A* **57**, 1906–1911 (1998).
- 24. Kerker, M. *The Scattering of Light and Other Electromagnetic Radiation*. (Academic Press, 1969).
- 25. Tanyag, R. M. P. *et al.* Communication: X-ray coherent diffractive imaging by immersion in nanodroplets. *Struct. Dyn.* **2**, 1–9 (2015).
- 26. Osipov, T. *et al.* The LAMP instrument at the Linac Coherent Light Source free-electron laser. *Rev. Sci. Instrum.* **89**, 1–10 (2018).
- 27. Ferguson, K. R. *et al.* The Atomic, Molecular and Optical Science instrument at the Linac Coherent Light Source. *J. Synchrotron Radiat.* **22**, 492–497 (2015).
- 28. Maximilian Jakob Bucher. Ultrafast Dynamics of Nanoparticles in Highly Intense X-Ray Pulses. (2017).
- 29. Gomez, L. F., Loginov, E., Sliter, R. & Vilesov, A. F. Sizes of large He droplets. *J. Chem. Phys.* **135**, 1–9 (2011).
- 30. Donnelly, R. J. & Barenghi, C. F. The observed properties of liquid helium at the saturated vapor pressure. *J. Phys. Chem. Ref. Data* **27**, 1217–1274 (1998).
- 31. Reinhard, P. & Suraud, E. B Gross properties of atoms and solids. in *Introduction to Cluster Dynamics* 259–266 (2004).
- 32. Bernando, C. *et al.* Shapes of rotating superfluid helium nanodroplets. *Phys. Rev. B* **95**, 1–14 (2017).
- 33. Attwood, D. & Sakdinawat, A. *X-rays and Extreme Ultraviolet Radiation: Principles and Applications.* (Cambridge University Press, 2016).
- 34. Henke, L. B., Gullikson, E. M. & Davis, J. C. X-ray interactions: photoabsorption, scattering, transmission, and reflection at E=50-30000 eV, Z=1-92. *At. Data Nucl. Data Tables* **54**, 181–342 (1993).

- 35. Erk, B. *et al.* Observation of shells in coulomb explosions of rare-gas clusters. *Phys. Rev. A At. Mol. Opt. Phys.* **83**, 1–5 (2011).
- 36. Murphy, B. F., Hoffmann, K., Belolipetski, A., Keto, J. & Ditmire, T. Explosion of xenon clusters driven by intense femtosecond pulses of extreme ultraviolet light. *Phys. Rev. Lett.* **101**, 1–4 (2008).
- 37. Ishikawa, K. & Blenski, T. Explosion dynamics of rare-gas clusters in an intense laser field. *Phys. Rev. A At. Mol. Opt. Phys.* **62**, 1–11 (2000).
- 38. Grech, M. *et al.* Coulomb explosion of uniformly charged spheroids. *Phys. Rev. E Stat. Nonlinear, Soft Matter Phys.* **84**, 1–10 (2011).
- 39. Katardjiev, I. V., Berg, S., Nender, C. & Miteva, V. On the impact parameter probability distribution in atomic collisions for Monte Carlo simulations. *Nucl. Inst. Methods Phys. Res. B* **72**, 28–32 (1992).